Int. J. Therm. Sci. (2001) 40, 969–980

S1290-0729(01)01283-2/FLA

Blowing models for cooling surfaces

Lionel Mathelin, Françoise Bataille, André Lallemand *

Centre de Thermique de Lyon, UMR 5008, Institut National des Sciences Appliquées de Lyon, Bât. 404, 20 av. A. Einstein, 69621 Villeurbanne cedex, France

(Received 17 October 2000, accepted 6 February 2001)

Abstract — To study the cooling of surfaces exposed to high temperature stress and heat flux, the blowing, or transpiration, technique is numerically investigated in the case of a porous circular cylinder. Two models are developed to simulate the blowing impact on the outer flow and an experimental set-up available allows for direct comparison and validation of the numerical simulations. The heat exchange occuring within the porous wall itself between the coolant and the solid part of the wall is accounted. The results show an excellent effectiveness of the blowing in terms of surface temperature reduction, even for low blowing ratii. The incident heat flux exhibits a maximum for medium blowing rates due to a decreasing heat transfer coefficient and a growing temperature difference between the surface and the main flow with the injection rate. Finally, the blowing is demonstrated to be very effective in cooling heavily thermally stressed parts in terms of homogeneity and coolant rate required. © 2001 Éditions scientifiques et médicales Elsevier SAS

blowing / cooling / cylinder / numerical simulations / boundary layer

Nomenclature

C_p	specific heat capacity	$J\cdot kg^{-1}\cdot K^{-1}$
D	outer cylinder diameter	m
d	cell center normal distance to the wall	m
F	blowing rate	
H	specific enthalpy	$J\cdot kg^{-1}$
h	vertical coordinate	m
h_{int}	internal heat transfer coefficient	$W\cdot m^{-3}\cdot K^{-1}$
h_{ext}	external convective heat transfer coefficient	$W\cdot m^{-2}\cdot K^{-1}$
k	turbulent kinetic energy	$m^{-2}\cdot s^{-2}$
l_μ	length scale for μ	m
l_ε	length scale for ε	m
n	normal coordinate	m
n_p	number of cells around the cylinder periphery	
Nu	Nusselt number	
$\mathcal{P}$	instantaneous pressure	Pa
p	fluctuating pressure	Pa
R	cylinder radius	m
r	radial coordinate	m
Re	Reynolds number	
Re_p	pore Reynolds number	
St	Stanton number	
S	source term	
T	temperature	K
T_m	matrix temperature	K
T_f	coolant temperature	K
t	time	s
U	mean velocity	$m\cdot s^{-1}$
$\mathcal{U}$	instantaneous velocity	$m\cdot s^{-1}$
u	fluctuating velocity	$m\cdot s^{-1}$
x	streamwise coordinate	m
y	transverse coordinate	m

Greek letters

δt	time step	s
δt^*	non dimensional time step	
δ_{ij}	Kronecker symbol	
ε	turbulent kinetic energy dissipation rate	$m^2\cdot s^{-3}$
η	thermal effectiveness	
θ	angle along the cylinder periphery	°
κ	von Kármán constant = 0.42	
λ	thermal conductivity	$W\cdot m^{-1}\cdot K^{-1}$
μ	dynamic viscosity	$kg\cdot m^{-1}\cdot s^{-1}$
ν	kinematic viscosity	$m^2\cdot s^{-1}$
ρ	density	$kg\cdot m^{-3}$

* Correspondence and reprints.
E-mail addresses: mathelin@cethil.insa-lyon.fr (L. Mathelin), daumas@cethil.insa-lyon.fr (F. Bataille), a.lal@cethil.insa-lyon.fr (A. Lallemand).

σ_k	turbulent Prandtl number for the turbulent kinetic energy	
τ_{ij}	stress tensor	Pa
φ	incident circumference-averaged convective heat flux	$W{\cdot}m^{-2}$
Φ	pressure strain tensor	$Pa{\cdot}s^{-1}$

Superscripts

–	time-averaged

Subscripts

f	fluid
∞	free stream fluid
inj	injected fluid
int	internal
m	matrix
t	turbulent
w	wall

1. INTRODUCTION

The need for always more powerful and efficient turbines lead to growing requirements in the mechanical strength and the thermal stress of the parts. High performances turbines imply a combustion temperature in the thermodynamical cycle as high as possible. Thus, the first turbine stages and the combustion chamber are heavily thermally stressed and an efficient cooling is necessary to maintain their mechanical properties. Many ways exist for the thermal protection of the turbine blades or the combustion chamber walls. The film cooling is the most widely used for aircraft engines and large scale gas turbines ([1–3] among many others) but others methods are also used for heavily stressed parts such as the impingement technique, where the turbine blades are hollow and a coolant flows internally through discrete holes and impact the inner surface of the outer coating [4]. Many studies have been conducted on the film cooling about the influence of the injection angle, the holes arrangement, the diameter or the shape of the holes. These parameters have been proved to influence the thermal performances but all these commonly used techniques present the drawback of requiring a large quantity of coolant, usually coming from the compressor and thus decreasing the overall efficiency. An alternative possibility is to blow a coolant through a porous wall, the so-called transpiration cooling technique, which is the limiting case of film cooling through tiny holes. In certain cases, the transpiration cooling can even been applied with a phase change (liquid transpiration) to take advantage from the enthalpy variation of the phase change [5]. Nevertheless, very few studies have been conducted on the transpiration cooling and most of them concern the flat plate geometry along with an experimental approach [6–9]. As far as the authors know, no studies deal about the numerical simulation of the transpiration cooling for the prediction of the thermal performances of a cylinder.

In this paper, the cooling efficiency of the complete blowing through a porous circular cylinder is numerically investigated. The internal heat transfer occuring in the porous medium is taken into account and the simulations are compared to experimental data for validation. After a description of the numerical methods and the experimental configuration, the models proposed for the transpiration cooling are presented in Section 4 and the internal heat exchange coupling in Section 5. Results are presented and discussed in Section 6.

2. NUMERICAL APPROACH

2.1. General configuration

The numerical approach chosen is to use a RANS solver code (Fluent©) in a 2-D configuration. Three-dimensional effects are believed to have a negligible impact on the surface temperature, especially in the most exposed part of the cylinder, i.e., the upstream part. This is supported by experimental measures of the wall temperature which do not exhibit any z dependance. Furthermore, the 3-D instability mode of the wake in this range of Reynolds numbers (mode B, [10]) takes place at a finite distance to the wall, in the vortices braid region. It is expected to have a negligible influence on the surface flow characteristics. This conclusion seems to be supported by preliminary results of 3-D computations currently in progress.

An unstructured mesh is used and extensive tests have been carried-out to ensure results independance from the grid. The numerical domain extent influence was investigated to check the blockage effect and the number of cells along the cylinder periphery (n_p) was varied from 80 to 3000 to reach the actual size of the pores. No effect has been noted on the results. The grid finally retained for computations is a 49 000 triangular-cell mesh, 20 cylinder diameters (D) long and 10 D wide, featuring 580 cells along the cylinder surface (see *figure 1*).

A prescribed static pressure is applied at the inlet section and the total mass flow rate is imposed at the outlet. Although the latter is not a non-reflective boundary conditions, no upstream disturbances occured.

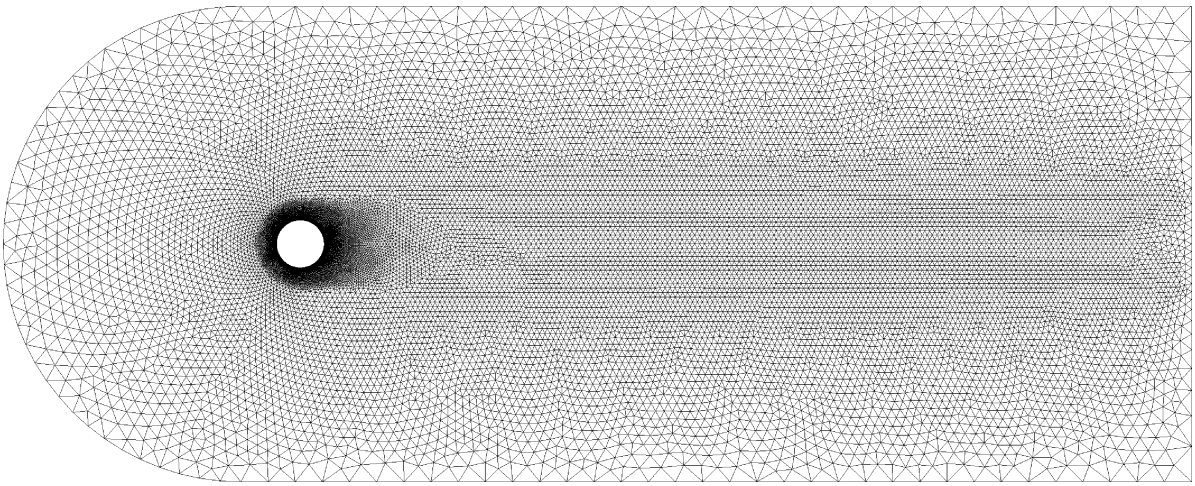

Figure 1. Mesh used for computations. 49 000 cells, 20 D long, 10 D wide, 580 cells around the cylinder.

Lateral boundary conditions are symmetry planes. An upwind second order scheme in space and a second order implicit formulation for the unsteady computations were used. The time step was chosen to have around 1000 time steps per vortex shedding period, i.e., $\delta t^* = \delta t U_\infty / D = 3 \times 10^{-3}$. The computations were run until, at least, 10 periods of vortex shedding occured, to allow a steady state to be reached. They were run on a DEC PWS clocked at 433 MHz and a DEC 4100 cluster clocked at 400 MHz, allowing for an efficient parallel processing.

The simulations range from Reynolds numbers of 500 to 7000, with the Reynolds number *Re* defined as follows:

$$Re = \frac{\rho_\infty U_\infty D}{\mu_\infty} \tag{1}$$

For Reynolds numbers higher than 500, the near wake of the cylinder becomes turbulent [10, 11] and a turbulence treatement has to be applied.

2.2. Computational methods

2.2.1. Governing equations

The Navier–Stokes equations, along with the energy equation, are solved in their time-dependent form:

$$\frac{\partial}{\partial t}\rho + \frac{\partial}{\partial x_i}(\rho \mathcal{U}_i) = 0 \tag{2}$$

$$\frac{\partial}{\partial t}(\rho \mathcal{U}_i) + \frac{\partial}{\partial x_j}(\rho \mathcal{U}_i \mathcal{U}_j) = -\frac{\partial}{\partial x_i}\mathcal{P} + \frac{\partial}{\partial x_j}\tau_{ij} \tag{3}$$

$$\frac{\partial}{\partial t}(\rho H) + \frac{\partial}{\partial x_i}(\rho \mathcal{U}_i H) = \frac{\partial}{\partial x_i}\left(\lambda \frac{\partial}{\partial x_i} T\right) \tag{4}$$

where the stress tensor τ_{ij} is given by

$$\tau_{ij} = \left[\mu\left(\frac{\partial}{\partial x_j}\mathcal{U}_i + \frac{\partial}{\partial x_i}\mathcal{U}_j\right)\right] - \frac{2}{3}\mu \frac{\partial}{\partial x_l}(\mathcal{U}_l)\delta_{ij} \tag{5}$$

The velocity $\mathcal{U}$ is decomposed into its mean part U and its fluctuating part u following the Reynolds decompositon theory. The turbulence is treated with a Reynolds Stress Model (RSM) and a low-Reynolds number approach to account for wall effects. The low-Reynolds number model retained accounts for the desequilibrium between production and dissipation of the turbulent kinetic energy within the boundary layer. The exact Reynolds stress transport equation is as follows

$$\begin{aligned}
&\frac{\partial}{\partial t}\left(\rho \overline{u_i u_j}\right) + \frac{\partial}{\partial x_k}\left(\rho U_k \overline{u_i u_j}\right) \\
&\quad = -\frac{\partial}{\partial x_k}\left[\rho \overline{u_i u_j u_k} + \overline{p(\delta_{kj} u_i + \delta_{ik} u_j)}\right] \\
&\qquad + \frac{\partial}{\partial x_k}\left[\mu \frac{\partial}{\partial x_k}\left(\overline{u_i u_j}\right)\right] \cdots \\
&\qquad - \rho\left(\overline{u_i u_k}\frac{\partial}{\partial x_k}U_j + \overline{u_j u_k}\frac{\partial}{\partial x_k}U_i\right) \\
&\qquad + \overline{p\left(\frac{\partial}{\partial x_j}u_i + \frac{\partial}{\partial x_i}u_j\right)} - 2\mu\,\overline{\frac{\partial}{\partial x_k}u_i \frac{\partial}{\partial x_k}u_j}
\end{aligned} \tag{6}$$

The turbulent viscosity μ_t is given by $\mu_t = \rho C_\mu k^2/\varepsilon$ with $C_\mu = 0.09$ and k the turbulent kinetic energy is given by the trace of the Reynolds stress tensor: $k =$

$\frac{1}{2}\overline{u_i u_i}$. The turbulent kinetic energy dissipation rate ε is defined as

$$\varepsilon = \nu \overline{\frac{\partial}{\partial x_j} u_i \frac{\partial}{\partial x_j} u_i} \tag{7}$$

and computed with a model transport equation similar to that of the standard k–ε model.

The turbulent diffusion is modeled using a simplified generalized gradient-diffusion model of Daly and Harlow [14]:

$$-\frac{\partial}{\partial x_k}\left[\rho\overline{u_i u_j u_k} + \overline{p(\delta_{kj}u_i + \delta_{ik}u_j)}\right] = \frac{\partial}{\partial x_k}\left(\frac{\mu_t}{\sigma_k}\frac{\partial}{\partial x_k}\left(\overline{u_i u_j}\right)\right) \tag{8}$$

Lien and Leschziner [13] derived a value of $\sigma_k = 0.82$ for the turbulent Prandtl number for k. For the pressure-strain, the model proposed by Gibson and Launder [14]; Fu et al. [15] and Launder [16, 17] is used. It reads:

$$\overline{p\left(\frac{\partial}{\partial x_j}u_i + \frac{\partial}{\partial x_i}u_j\right)} = \Phi_{ij,1} + \Phi_{ij,2} \tag{9}$$

where $\Phi_{ij,1}$ is the so-called "return-to-isotropy" term and $\Phi_{ij,2}$ the "rapid pressure-strain". $\Phi_{ij,1}$ is modeled as

$$\Phi_{ij,1} = -C_1\rho\frac{\varepsilon}{k}\left(\overline{u_i u_j} - \frac{2}{3}\delta_{ij}k\right) \tag{10}$$

while the rapid pressure-strain term is modeled as

$$\Phi_{ij,2} = -C_2\left[(P_{ij} + F_{ij} + G_{ij} - C_{ij}) - \frac{2}{3}\delta_{ij}(P + G - C)\right] \tag{11}$$

where P_{ij}, F_{ij}, G_{ij} and C_{ij} are respectively the stress production, the production by system rotation, the buyoancy production and the convection term of the Reynolds stress transport equation (6). $P = \frac{1}{2}P_{kk}$, $G = \frac{1}{2}G_{kk}$ and $C = \frac{1}{2}C_{kk}$.

C_1 and C_2 are functions of the Reynolds stress invariants and the turbulent Reynolds number, according to the suggestion of Launder and Shima [18]:

$$C_1 = 1 + 2.58A\sqrt{A_2}\left[1 - \mathrm{e}^{-(0.0067Re_t)^2}\right]C_2 = 0.75\sqrt{A} \tag{12}$$

with the turbulent Reynolds number defined as $Re_t = \rho k^2/(\mu\varepsilon)$ and where the parameter A and the tensor invariants A_2 and A_3 are

$$A = \left[1 - \frac{9}{8}(A_2 - A_3)\right] \tag{13}$$

$$A_2 = a_{ik}a_{ki} \tag{14}$$

$$A_3 = a_{ik}a_{kj}a_{ji} \tag{15}$$

a_{ij} is the anisotropic part of the Reynolds stress tensor defined as

$$a_{ij} = -\left(\frac{-\rho\overline{u_i u_j} + 2/3\rho k\delta_{ij}}{\rho k}\right) \tag{16}$$

2.2.2. Boundary conditions treatement

The near wall model consists in considering two different regions in the boundary layer: a viscosity-affected region and a fully-turbulent region, whose demarcation is determined by the wall-distance-based, turbulent Reynolds number Re_d, defined as $Re_d = \frac{\rho\sqrt{k}d}{\mu}$ where d is the normal distance from the wall at the cells centers. The viscosity-affected near-wall region ($Re_d < 200$) is resolved all the way down to the viscous sublayer using the one-equation model of Wolfstein [19], while in the fully turbulent region, i.e., $Re_d > 200$, the RSM model is employed. The momentum and k equations are retained, but the turbulent viscosity, μ_t, is computed from $\mu_t = \rho C_\mu\sqrt{k}\,l_\mu$. The ε field is computed from $\varepsilon = k^{3/2}/l_\varepsilon$. From [20], the length scales that appear are computed as follows:

$$l_\mu = c_l n\left[1 - \mathrm{e}^{(-Re_d/A_\mu)}\right] \tag{17}$$

$$l_\varepsilon = c_l n\left[1 - \mathrm{e}^{(-Re_d/A_\varepsilon)}\right] \tag{18}$$

The constants are $c_l = \kappa C_\mu^{-3/4}$, $A_\mu = 70$, $A_\varepsilon = 2c_l$ where κ is the von Kármán' constant ($\kappa = 0.42$).

3. EXPERIMENTAL FACILITIES

An experimental set-up is used for the validation of the numerics. The experiments are conducted using a heated subsonic wind-tunnel. A sketch of the experimental facility is given in *figure 2*. The cross section is 0.2 m × 0.5 m and the velocity can be varied up to 30 m·s^{-1}. Thanks to 120 kW electrical heating needles, the main flow temperature ranges from ambient to 300 °C. The hollow cylinder used is 16.2 mm in outer diameter, 2.1 mm thick and 320 mm long, leading to a blockage and aspect ratii of 8.1% and 20, respectively. It is made of sintered stainless steel, whose porosity is about 33% and with pores of 30 μm in diameter typically. The cylinder is fed by the ends with a secondary fluid (coolant), at

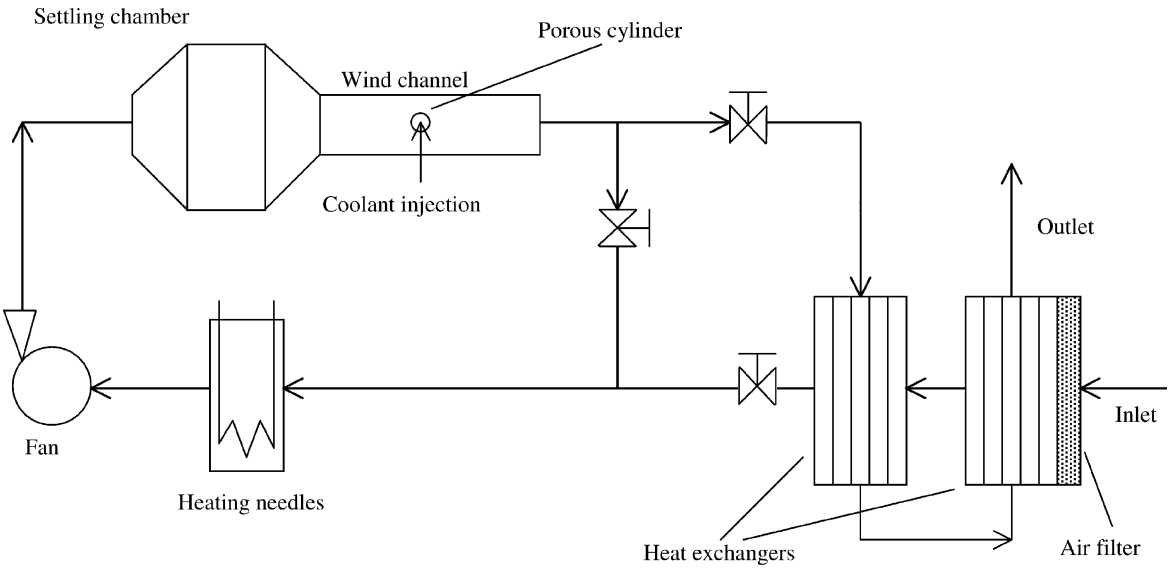

Figure 2. Schematic of the test facility. Experiments are carried-out in an open-loop configuration.

ambient temperature, which flows outwards the cylinder surface. To prevent from end effects, oblong end plates are used, consisting in a rectangle featuring 5 D in length upstream to the cylinder axis, 15 D downstream and 10 D in height.

The dynamical and thermal profiles are obtained using both hot and cold wire probes. *Figure 3* shows the experimental arrangement of the probes and the working coordinates system. The velocity is measured with a single hot wire Dantec 55P11-2 probe driven by a 90C10 CTA Dantec module. Because of the very thin boundary layer thickness investigated (e.g., around 600 μm for $Re = 7000$), the single hot wire probe was preferred to the much more intrusive and larger X-wires probe. The wires are made of 10% rhodium–platinum, 10 μm in diameter and 1.5 mm long. The temperature profiles are measured with a 5 μm Wollaston (platinum–rhodium core and silver coating) cold wire probe. More details about the probe calibration both in velocity and temperature can be found in [21]. The cylinder surface temperature is obtained with K-type thermocouples, 0.1 mm in diameter, welded onto the surface. The use of an IR camera has proved that the thermocouples do not distord the temperature field of the surface [22]. Hot wires are calibrated in velocity with a Pitot tube combined with a high sensitivity Furness FCO332 differential pressure transmitter. Its accuracy is better than 1% throughout its [0–100] Pa range with a 0.1 Pa resolution. The uncertainty of the Reynolds number thus varies from 0.7 to 5.5% depending on the operating conditions. The uncertainty on the blowing ratio, defined below, is typically of the order of 7% and always below 10% for all experimental conditions.

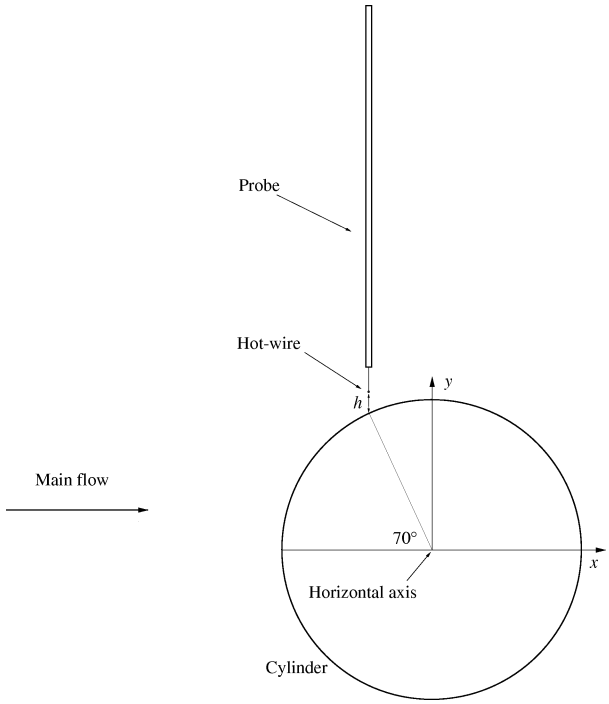

Figure 3. Probe arrangement and coordinates system.

4. MODELS FOR BLOWING

The blowing impact is studied in terms of the blowing rate, F, defined as

$$F = \frac{\rho_{\text{inj}} U_{\text{inj}}}{\rho_\infty U_\infty} \tag{19}$$

To model the secondary fluid flowing through the porous surface of the cylinder, two different approaches are used. The injection is supposed to be uniform throughout the whole surface and normal to the wall. The model then must account for the viscous drag, together with the mass, momentum and enthalpy generation from the injected fluid. The physical phenomenon is directly modeled, instead of using additional terms in the wall functions as previously done [8, 23–28]. The first model, hereafter denoted the holes model, consists in a succession of impermeable wall segments and holes where a normal velocity is imposed (*figure 4*). The actual porosity (33%) is preserved as the holes width is half the wall segments length and the secondary fluid is made to flow through the holes. Their size was varied to check independence of the results from this parameter and was decreased down to its actual size (about 30 μm). No influence of the holes size or of the number of cells was noted. This model has been tested and validated in the case of a flate plate geometry by Bellettre et al. [29] and was proved to give excellent results in this configuration. However, the circular cylinder involves much higher gradients than a developped boundary layer over a flat plate and, for high blowing ratii, the holes model can present some discontinuities. The succession of boundary conditions can lead to discontinuous values above the surface and this claims for another model, hereafter denoted the sources model. It consists in a continuous impermeable wall just above which a mass, momentum and heat source is applied at the centroid of the first cell (*figure 4*). If the cell size is negligible compared to the cylinder radius and the boundary layer thickness, it can be considered to have an identical impact on the outer flow. The momentum is set in each cell to always have a normal direction along the whole periphery of the cylinder. The sources expressions for the different variable are the following:

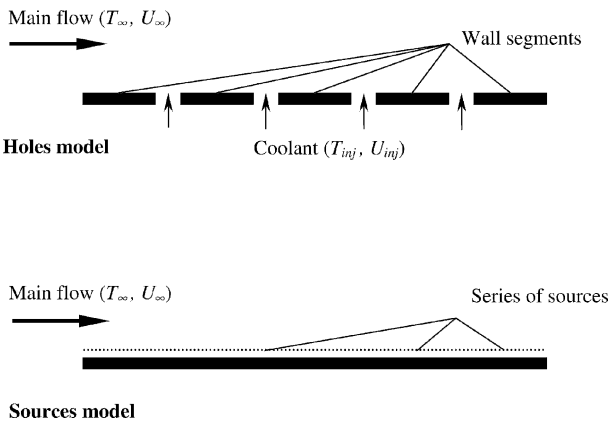

Figure 4. Schematics of the holes and sources models configuration.

$$S_{\text{mass}} = \rho_{\text{inj}} U_{\text{inj}} \frac{2\pi R}{n_{\text{p}}} \tag{20}$$

$$S_{\text{momentum}} = \rho_{\text{inj}} U_{\text{inj}}^2 \frac{2\pi R}{n_{\text{p}}} \tag{21}$$

$$S_{\text{energy}} = \rho_{\text{inj}} U_{\text{inj}} C p_{\text{inj}} T_{\text{inj}} \frac{2\pi R}{n_{\text{p}}} \tag{22}$$

The holes and the sources models will be used for studying the blowing impact on the flow and the wall temperature.

5. INTERNAL COUPLING

The numerical modeling described so far concerns the flow outer the cylinder wall but the wall boundary conditions (surface temperature, injected fluid temperature) need to be specified. Their determination requires a model for the flow within the porous wall. As the coolant fluid flows through the porous matrix of the cylinder, it heats up due to internal heat exchange with the hot solid part of the wall. This cools down the inner wall and thus the cylinder surface by heat conduction and tends to increase the radiative heat transfer from the hot ceiling and windows of the wind-tunnel. Moreover, the temperature of the coolant injected in the boundary layer is higher than ambient due to internal heat transfer and this tends to decrease the thermal protection effectiveness. Consequently, the coupling between the inner and the outer flow has to be taken into account to allow for validation of computations with experimental data. To model this internal heat exchange, a subroutine is linked to the flow simulation. The dynamical and thermal equations of the coolant flowing through the matrix, along with the temperature distribution of the solid part of the wall, are computed using a finite differences code onto a 25-cell thick mesh matching the actual geometry of the wall (thickness of 3 mm). This reduces to a flow rate imposed 2-equation system and specific boundary conditions:

$$(\rho_{\text{inj}} U_{\text{inj}}) C p_{\text{inj}} \frac{\partial T_{\text{f}}(r)}{\partial r} = h_{\text{int}}(r)\big(T_{\text{m}}(r) - T_{\text{f}}(r)\big) \tag{23}$$

$$\lambda \frac{\partial^2 T_{\mathrm{m}}(r)}{\partial r^2} = h_{\mathrm{int}}(r)\big(T_{\mathrm{m}}(r) - T_{\mathrm{f}}(r)\big) \tag{24}$$

where $h_{\mathrm{int}}(r)$ is a linear function of the radius to account for the decreasing velocity within the porous material and λ is the equivalent thermal conductivity accounting for the porosity effects. Its value is governed by the following correlation, established from experiments [22]:

$$Nu_{\mathrm{int}} = 0.037 Re_{\mathrm{p}} \tag{25}$$

where Re_{p} is based on the pores diameter and the local fluid velocity and properties. The value of the heat transfer coefficient was proved not to be crucial as a $\pm 20\%$ variation lead to less than 6% of variation in the Stanton number for a blowing ratio of 2% and almost no change in the thermal effectiveness. The cylindrical geometry and the variation of the coolant temperature along its path throughout the wall make its properties and its velocity to change with space. The boundary conditions are a prescribed inlet coolant temperature at the inner radius, a fixed convective heat transfer coefficient in the inner surface of the porous material and a convective heat transfer coefficient at the outer surface of the cylinder. The subroutine thus prescribed the outer wall surface and the coolant exit temperature computed using the convective heat transfer coefficient determined from the code as a boundary condition.

6. RESULTS

In this range of Reynolds number, the wake of the cylinder exhibits a periodic vortex shedding. This phenomenon is observed in our unsteady computations and are in good agreement with experimental results [30]. When blowing is applied, the vortex shedding frequency decreases. Furthermore, we observed an important coupling between the dynamical and thermal aspects as shown in *figure 5* where the temperature contours are plotted. It is seen that the cold fluid is carried downstream in the core of the vortices. Nevertheless, this aspect will not be further detailled here as it is not the purpose of the present paper.

In the following sections, results are presented about the velocity and temperature profiles in the boundary layers along with surface temperature evolution with blowing. The emphasize is also put on the comparison between experimental data and results from the numerical simulations.

6.1. Dynamical and thermal profiles

Figure 6 shows an isothermal time-averaged velocity magnitude profile at an angle of 65° refered from the front stagnation point with both experimental and numerical data. The plot direction is vertical for experimental convenience. Due to experimental constraints, the profiles are truncated below a certain distance to the wall (around 160 μm).

Both numerical models (holes models and sources models) give a very similar profiles and only the results from the sources model are presented for convenience. The numerical profiles are in good agreement with the experimental data. When the blowing ratio is increased, the boundary layer thickness tends to increase as well, leading to a lower velocity gradient in the immediate vicinity of the surface and thus, to a decrease in the viscous drag. The blowing promotes the boundary layer separation to a lower angle and tends to widen the wake. A similar trend can be noted from *figure 7* where the velocity magnitude profile along the vertical direction

Figure 5. Temperature contours in the wake.

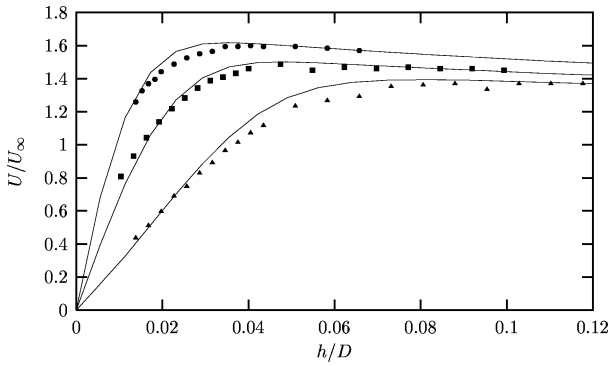

Figure 6. Velocity magnitude profile at $\theta = 65°$ along the vertical direction. $T_\infty =$ ambient. Symbols are experimental data; •, $F = 0\%$; ■, $F = 2\%$; ▲, $F = 5\%$. Numerical results using the sources model are the corresponding solid lines.

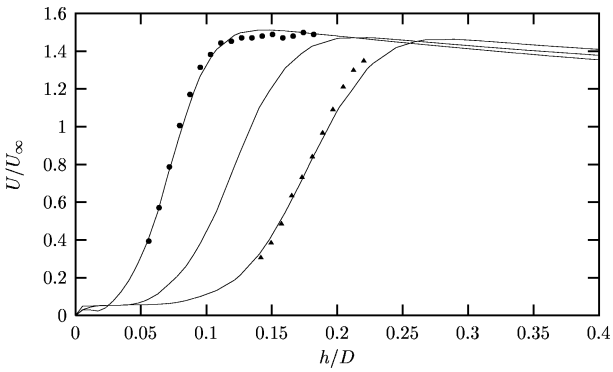

Figure 7. Velocity magnitude profile at $\theta = 105°$ along the vertical direction using the sources model. $T_\infty =$ ambient. Symbols are experimental data; •, $F = 0\%$; ▲, $F = 5\%$. Numerical results using the sources model are the corresponding solid lines plus the plot for $F = 2\%$ where no experimental data are available.

is plotted at an angle of 105°. The dead fluid zone, below the separated boundary layer, hereafter denoted the shear layer, is clearly visible from the low velocity region. It corresponds to a recirculating zone, occuring just beyond the separation point. The recirculating point location oscillates in time at the back of the cylinder and, when time-averaged over a vortex shedding period, the flow does not recirculate, i.e., the streamwise velocity remains positive throughout the profile.

Figure 8 shows a similar plot for the temperature profile at an angle of 65°. The main stream is at a 473 K temperature while the coolant is at an ambient temperature. Same conclusions can be drawn from the plot as for the dynamical boundary layer. The thermal boundary layer thickness increases and the temperature gradient at the surface decreases, leading to a lower convective heat transfer coefficient in case of blowing. When the blowing gets stronger, the profile tends to be *S*-shaped, exhibiting the promotion of the separation. Below the separated boundary layer, a stationary cold recirculating zone is present and leads to a local minimum in the surface temperature and the convective heat transfer.

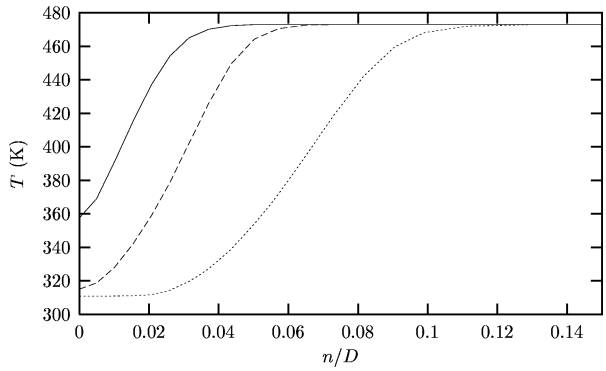

Figure 8. Temperature normal profile at $\theta = 65°$. $T_\infty = 473$ K. Solid line, $F = 2\%$; semi-dashed line, $F = 5\%$; dashed-line, $F = 10\%$.

6.2. Thermal stress

Due to different dynamics, the thermal stress is non-uniform along the cylinder surface. In the upstream part, the boundary layers tend to be "squashed" onto the surface, leading to strong gradients and transfer coefficients and is thus the most stressed portion. *Figure 9* shows the time-averaged thermal effectiveness as a function of the angle along the cylinder periphery with the sources model. The effectiveness η, defined as

$$\eta = \frac{T_\infty - T_\mathrm{w}}{T_\infty - T_\mathrm{inj}} \tag{26}$$

where T_∞, T_w and T_inj are the main flow, surface and coolant temperature respectively, exhibits a minimum for low angles, near the front stagnation point as expected. It increases along the upstream boundary layer due to the growing thermal boundary layer and the corresponding decrease in the convective heat transfer. Beyond the boundary layer separation, a cold recirculating zone is present between the surface and the shear layer and leads to a local maximum in the effectiveness evolution. At the back of the cylinder, strong recirculations draw some hot fluid from the main stream to the rear back of the cylinder and the effectiveness sharply decreases again. This is in full agreement with the first experimental data on blowing [31].

Figure 10 shows the evolution of the effectiveness with the blowing rate. It clearly exhibits an exponential behavior, tending to an asymptotic value. The numerical results are in good agreement with experimental data, validating the reliability of the surface temperature and the wall heat flux computation procedure, both used in the subroutine to determine the internal energy balance. Nevertheless, the holes model results depart from the experimental curve for low blowing ratii. This is due to a different mixing between the coolant and the main fluid above the surface. In the case of the holes models, the jets flowing out from the holes penetrate deep inside the boundary layer while in the sources models the mixing occurs in the first cell. Moreover, the holes model is discrete in terms of boundary conditions, which is not the case with the sources model where the boundary condition is uniform. In the case of the flat plate where the holes model was validated, the gradients involved are low compared to the upstream part of a circular cylinder and these differences do not play an important role.

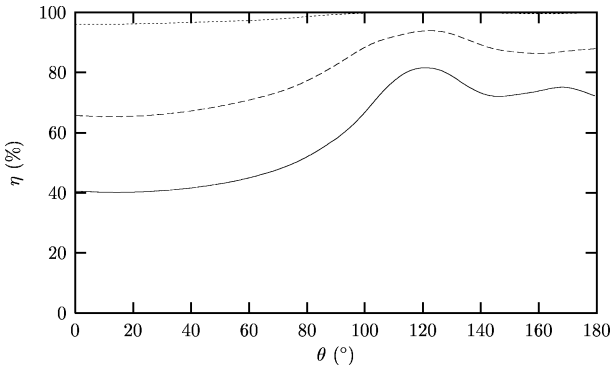

Figure 9. Thermal effectiveness along the cylinder periphery. $T_\infty = 473$ K. Solid line, $F = 1\%$; semi-dashed line, $F = 2\%$; dashed-line, $F = 5\%$.

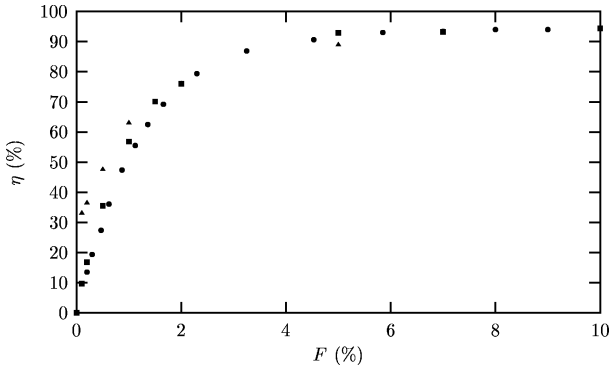

Figure 10. Thermal effectiveness as a function of the blowing rate at $\theta = 65°$. $T_\infty = 473$ K. ●, experimental data; ■, sources model; ▲, holes model.

Additional tests tend to suggest that for this particular result, the mesh density, i.e., the holes diameter, could have a small influence which is not the case for the sources model. Because of its more physically relevant features, only results from the sources model will be presented in the following. Due to radiative heat transfer, the experimental curve does not reach the value of 1 although the convective heat transfer is nil for blowing ratii higher than 5%. One of the major advantages of the blowing over the film cooling is the occurence of a strong heat transfer within the wall to be protected, due to a large volumic heat transfer coefficient. This hardly occurs with the film cooling where the exchange area between the coolant and the wall is very low.

In *figure 11*, the circumference-averaged convective incident heat flux is plotted as a function of the blowing rate. When no blowing is applied, the cylinder is considered as adiabatic and the incident heat flux is nil. When the coolant flows through the cylinder wall, the matrix temperature is not uniform any more and a conductive heat flux occurs, decreasing the outer surface temperature. The external heat flux thus increases, while the convective heat transfer coefficient decreases due to a growing thermal boundary layer. Beyond a certain amount of blowing, the external convective transfer is low, the internal transfer coefficients between the coolant and the wall are very high and only radiative transfer occurs on the external surface but it is remains weak due to the low temperature configuration studied. Consequently, after a maximum obtained for 1.5% of injection approximately, the heat flux is dramatically reduced with the blowing.

From *figures 10* and *11*, the periphery-averaged Stanton number, *St*, evolution with blowing can be evaluated

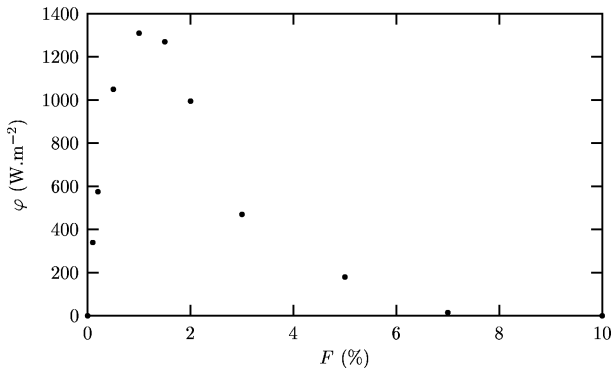

Figure 11. Incident circumference-averaged convective heat flux as a function of the blowing rate. $T_\infty = 473$ K.

and is plotted in *figure 12*. It is defined as

$$St = \frac{h_{\text{ext}}}{\rho_\infty U_\infty C p_\infty} \tag{27}$$

and exhibits a monotonuous decrease with F as expected from the growing thermal boundary layer and the decreasing heat transfer coefficient. The Stanton number is thus reduced by a factor of two for a blowing rate of 1.5% only and decreases down to roughly zero for $F > 6\%$.

Figure 13 exhibits the thermal desequilibrium (difference of temperature) between the coolant as it flows from the porous matrix and the external cylinder surface. The desequilibrium is far from zero for low blowing rates ($F < 3\%$), thus clearly claiming for this phenomenon to be accounted for in the different numerical or theoretical approaches where it can not be neglected. As the blowing gets stronger, the volumic heat transfer coefficient between the porous matrix and the coolant increases and the external surface temperature decreases leading to lower thermal gradients and a lower desequilibrium.

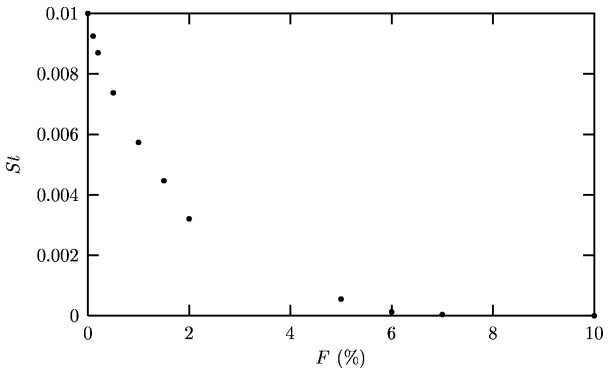

Figure 12. Stanton number as a function of the blowing rate. $T_\infty = 473$ K.

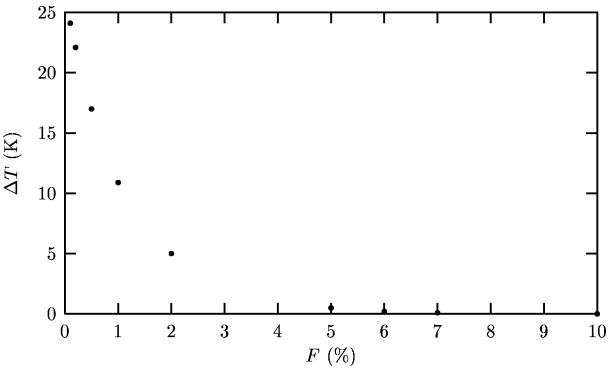

Figure 13. Temperature difference between the coolant injected into the main flow and the cylinder surface: the thermal desequilibrium. $T_\infty = 473$ K.

6.3. Optimisation

As seen from *figure 9*, an uniform blowing along the cylinder periphery leads to a non-uniform effectiveness, thus to a non-optimum configuration in terms of coolant rate savings. In turbine facilities, it is essential to reduce the coolant flow rate required to achieve better overall performances and this strongly supports the search for an optimum distribution of the blowing. The criterion for such an optimized distribution imposed that the effectiveness should not depart of more than 5% from its circumference-averaged value. Its evolution along the surface is plotted in *figure 14* and the corresponding blowing rate distribution can be seen in *figure 15*. The blowing needs to be strong in the upstream part of the cylinder because of the high heat transfer coefficient. As the angle increases, the thermal boundary layer grows and the required blowing rate decreases up to the separation point where the recirculations lead for the need of a higher blowing rate.

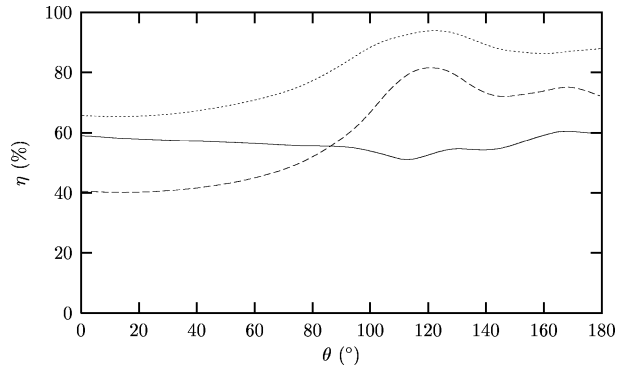

Figure 14. Thermal effectiveness along the cylinder periphery. $T_\infty = 473$ K. Solid line, optimized blowing distribution; semi-dashed line, uniform 1% blowing; dashed-line, uniform 2% blowing.

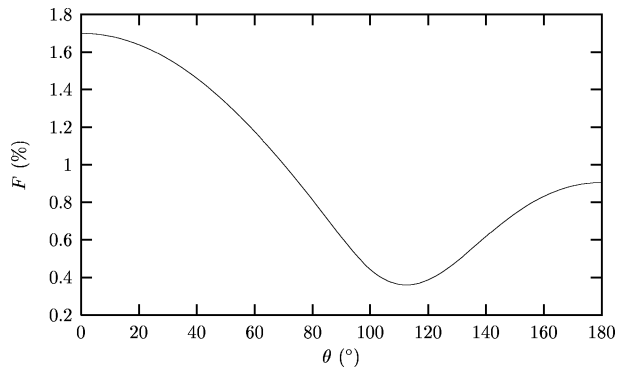

Figure 15. Optimized blowing distribution along the periphery. Circumference-averaged $F = 0.85\%$.

The equivalent uniform blowing rate (i.e., periphery-averaged) of the optimized solution is about 0.85%, providing a thermal effectiveness always higher than 52% whatever the angle θ. Using an uniform blowing, this level of thermal protection would require a blowing ratio of roughly 1.5%, clearly exhibiting the benefits from the optimized configuration.

7. CONCLUDING REMARKS

The numerical study of the blowing through a porous circular cylinder in cross-flow reveals the effectiveness of this technique in protecting mechanical parts submitted to a high thermal stress. The blowing is proved to be reliably simulated using the numerical models as proved by comparisons with experiments, especially the sources model which was found to handle even with very strong gradients. These results allow to use the numerical simulation for the design of new turbine systems and to predict their thermal load.

The blowing through a porous surface was seen to thicken the boundary layers, both dynamical and thermal, and to lower the gradients. The wall temperature is kept to reasonable levels, even with low blowing ratii, taking advantage from its "smoothness" compared to other techniques (like film cooling) and from the high heat exchange area within the porous matrix itself. This gives a structural advantage to the transpiration cooling and allows for much lower blowing ratii required for a given protection. A better effectiveness can be achieved optimizing the blowing rate distribution around the periphery to account for varying heat transfer coefficient along the surface. A further coolant flow rate saving of a factor of 2 approximately can then be obtained compared to the case of an uniform blowing. The thermal desequilibrium between the coolant and the porous matrix is found to be far from negligible for low injection rates, while tending to zero for high blowing as the internal heat transfer coefficient increases. This phenomenon should thus be accounted in the theoretical and numerical studies.

REFERENCES

[1] Lee S.W., Kim Y.B., Lee J.S., Flow characteristics and aerodynamics losses of film-cooling jets with compounds angle orientations, J. Turbomach. 119 (1997) 310–319.

[2] Goldstein R.J., Stone L.D., Row-of-holes film cooling of curved walls at low injection angles, J. Turbomach. 119 (1997) 574–579.

[3] Ekkad S.V., Han J.C., Du H., Detailled film cooling measurements on a cylindrical leading edge model: effect of free-stream turbulence and coolant density, J. Turbomach. 120 (1998) 799–807.

[4] Facchini B., Ferrara G., Innocenti L., Blade cooling improvement for heavy duty gas turbine: the air coolant temperature reduction and the introduction of stream and mixed steam/air cooling, Internat. J. Therm. Sci. 39 (1) (2000) 74–84.

[5] Bellettre J., Bataille F., Lallemand A., Prediction of thermal protection of walls by blowing with different fluids, Internat. J. Therm. Sci. 38 (6) (1999) 492–500.

[6] Whitten D.G., Moffat R.J., Kays W.M., Heat transfer to a turbulent boundary layer with non-uniform blowing and surface temperature, in: Proceedings of 4th Internat. Heat Transfer Conf., Versailles, France, 1970, 12 p.

[7] Moffat R.J., Kays W.M., The turbulent boundary layer on a porous plate: experimental heat transfer with uniform blowing and suction, Internat. J. Heat Mass Transfer 11 (10) (1968) 1547–1566.

[8] Simpson R.L., Characteristics of turbulent boundary layers at low Reynolds numbers with and without transpiration, J. Fluid Mech. 42 (1970) 769–802.

[9] Rodet J.C., Campolina França G.A., Pagnier P., Morel R., Lallemand A., Etude en soufflerie thermique du refroidissement de parois poreuses par effusion de gaz, Rev. Gen. Therm. 37 (2) (1998) 123–134.

[10] Williamson C.H.K., Vortex dynamics in the cylinder wake, Ann. Rev. Fluid Mech. 28 (1996) 477–539.

[11] Zdravkovich M.M., Flow Around Circular Cylinders. Vol 1: Fundamentals, Oxford Univ. Press, London, 1997.

[12] Daly B.J., Harlow F.H., Transport equations in turbulence, Phys. Fluids 13 (1970) 2634–2649.

[13] Lien F.S., Leschziner M.A., Assesment of turbulent transport models including non-linear RNG eddy-viscosity formulation and second-moment closure, Comput. Fluids 23 (8) (1994) 983–1004.

[14] Gibson M.M., Launder B.E., Grounds effects on pressure fluctuations in the atmospheric boundary layer, J. Fluid Mech. 86 (1978) 491–511.

[15] Fu S., Launder B.E., Leschziner M.A., Modeling strongly swirling recirculating jet flow with Reynolds-stress transport closures, 6th symposium on turbulent shear flows, Toulouse, France, 1997.

[16] Launder B.E., Second-moment closure and its use in modeling turbulent industrial flows, Internat. J. Num. Meth. Fluids 9 (1989) 963–985.

[17] Launder B.E., Second-moment closure: present... and future?, Internat. J. Heat Fluid Flow 10 (4) (1989) 282–300.

[18] Launder B.E., Shima N., Second-moment closure for the near-wall sublayer: development and application, AIAA J. 27 (10) (1989) 1319–1325.

[19] Wolfstein M., The velocity and temperature distribution of one-dimensional flow with turbulence augmentation and pressure gradient, Internat. J. Heat Mass Transfer 12 (1969) 301–318.

[20] Chen H.C., Patel V.C., Near-wall turbulence models for complex flows including separation, AIAA J. 26 (6) (1988) 641–648.

[21] Mathelin L., Bataille F., Lallemand A., Near wake of a circular cylinder submitted to blowing. Part I—Boundary layers evolution, Internat. J. Heat Mass Transfer 44 (2001) 3701–3708.

[22] Bellettre J., Bataille F., Rodet J.-C., Lallemand A., Thermal behavior of porous plates subjected to air blowing, AIAA J. Thermophys. Heat Transfer 14 (4) (2000) 523–532.

[23] Stevenson T.N., Inner region of transpired turbulent boundary layers, AIAA J. 6 (3) (1968) 553–554.

[24] Kays W.M., Heat transfer to the transpired turbulent boundary layer, Internat. J. Heat Mass Transfer 15 (1972) 1023–1044.

[25] Landis R.B., Mills F., The calculation of turbulent boundary layers with foreign gas injection, Internat. J. Heat Mass Transfer 15 (1972) 1905–1932.

[26] So R.M.C., Yoo G.J., Low Reynolds number modeling of turbulent flows with and without wall transpiration, AIAA J. 25 (1987) 1556–1564.

[27] Silva-Freire A.P., An asymptotic solution for transpired incompressible turbulent boundary layers, Internat. J. Heat Mass Transfer 31 (1998) 1011–1021.

[28] Campolina França G.A., Pagnier P., Lallemand A., Simulation des transferts de masse et de chaleur par modélisation à bas nombres de Reynolds dans un écoulement avec effusion locale en canalisation, Rev. Gén. Therm. 37 (3) (1998) 205–222.

[29] Bellettre J., Bataille F., Lallemand A., A new approach for the study of the turbulent boundary layer with blowing, Internat. J. Heat Mass Transfer 42 (1999) 2905–2920.

[30] Mathelin L., Bataille F., Lallemand A., Near wake of a circular cylinder submitted to blowing. Part II—Impact on the dynamics, Internat. J. Heat Mass Transfer 44 (2001) 3709–3719.

[31] Johnson B.V., Hartnett J.P., Heat transfer from a cylinder in crossflow with transpiration cooling, J. Heat Transfer (May 1963) 173–179.